SCIENCE CHINA
Information Sciences

• REVIEW •
Special Focus on Bistatic Synthetic Aperture Radar Signal Processing

June 2015, Vol. 58 061301:1–061301:20
doi: 10.1007/s11432-015-5334-6

Space-surface bistatic synthetic aperture radar with navigation satellite transmissions: a review

ANTONIOU Michail[1]*, CHERNIAKOV Mikhail[1] & MA Hui[1,2]

[1]*Electronic, Electrical and Systems Engineering Department, University of Birmingham, Birmingham* B152TT*, UK;*
[2]*School of Electronic and Information Engineering, Beihang University, Beijing* 100191*, China*

Received January 26, 2015; accepted March 12, 2015; published online April 28, 2015

Abstract This paper reviews the theory and practice of Space-Surface Bistatic Synthetic Aperture Radar (SS-BSAR) using navigation satellites as transmitters. In recent years, this innovative technology has reached a maturity stage which allows it to be considered for a wide range of applications. The paper covers the fundamental aspects of this technology as a radar system, such as the resolution, power budget and Point Spread Function (PSF) analysis, as well as its signal processing aspects and the state of the art in terms of advanced SAR techniques that it enables. Finally, the theoretical aspects of the paper may be directly transferred to the more generic SS-BSAR concept.

Keywords bistatic synthetic aperture radar, GNSS-based SAR, space-surface bistatic SAR, coherent change detection, multi-perspective imaging, multistatic imaging, spatial resolution improvement

Citation Antoniou M, Cherniakov M, Ma H. Space-surface bistatic synthetic aperture radar with navigation satellite transmissions: a review. Sci China Inf Sci, 2015, 58: 061301(20), doi: 10.1007/s11432-015-5334-6

1 Introduction

In order to address the diverse requirements for earth observation and surveillance applications, bistatic synthetic aperture radar (SAR) has seen growing focus by research community. Bistatic SAR is defined as a system that uses spatially separated transmitters and receivers [1,2]. Despite the additional system complexity, this spatial separation has opened new horizons to SAR research. For example, in terms of scientific progress, a bistatic acquisition may substantially increase the information space of monostatic SAR acquisitions by considering different target scattering angles, among other things. In terms of system topologies, the separation between the transmitting and receiving platforms offers different combinations between them, such as spaceborne [3] or airborne [4].

A special BSAR topology, Space-Surface BSAR (SS-BSAR) uses a spaceborne transmitter and a receiver located on or near the Earth's surface. Even this special topology offers a number of system configurations. The receiver can be on-board an aircraft, a ground moving vehicle or even fixed on the ground. On the other hand, the spaceborne segment can be a radar satellite or even a transmitter of opportunity [4,5].

* Corresponding author (email: m.antoniou@bham.ac.uk)

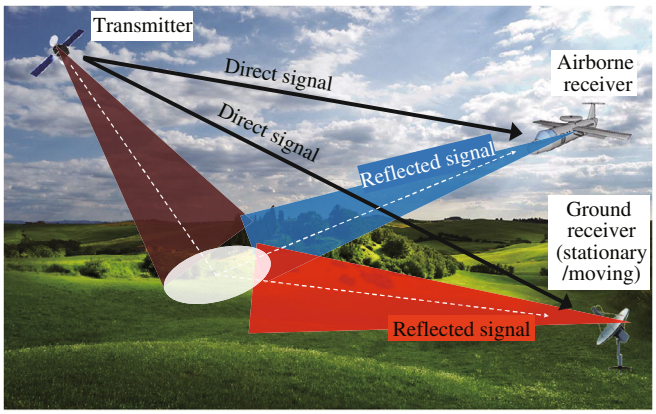

Figure 1 (Color online) The concept of GNSS-based passive SAR.

Perhaps the first record of an SS-BSAR experiment with a dedicated radar satellite was initiated in the United States [6]. However, since then major research on this topic has been performed both in Europe and in China. In Europe, the University of Siegen conducted experiments with the TerraSAR-X satellite (X-band), and using both airborne [7,8] and fixed [8,9] receivers in a number of publications. In parallel, similar experiments were conducted and reported for an airborne receiver by the German Aerospace (DLR). Figure 7a of [9] shows an example image obtained by the spaceborne/stationary bistatic topology. It is a detail of a bistatic SAR-image showing a factory 700 m away from the position of the stationary receiver, with the monostatic image in slant range geometry gathered by the satellite only (Figure 7b of [9]). An optical view of the scene (Figure 7c of [9]) is also given for comparison. The result was processed using a modified time domain processor using both receiving channels.

In China, the Beijing Institute of Technology (BIT) used China's YaoGan-1 SAR satellite [10] in SS-BSAR configurations. In [11], a modified nonlinear chirp scaling (NLCS) algorithm based on series reversion was proposed to deal with the space-variance problem for spaceborne/stationary configuration, where high-order NLCS perturbation items were introduced. The effectiveness of the proposed method was validated using a real spaceborne/stationary experiment carried out in Liangxiang, Beijing. The YaoGan-1 (an L-band spaceborne SAR satellite launched by China) was selected as the transmitter and the stationary receiver was mounted on top of a tall building [10]. The result was presented in Figure 13 of [11] and the difference from the monostatic YaoGan-1 SAR image (Figure 15 of [11]) was revealed.

Apart from SS-BSAR with dedicated spaceborne transmitters, SS-BSAR can also be passive, utilising illuminators of opportunity such as geostationary broadcast satellites [12], spaceborne/mobile communication signals [13–15] and Global Navigation Satellite Systems (GNSS) [16]. In this paper, we focus on the GNSS-based SAR.

In peer of those passive systems, GNSS-based bistatic SAR (Figure 1) has its unique peculiarities. In this technique, the option of GNSS transmitter can be GPS (US), GLONASS (RU), Beidou (China) and the Galileo (Europe) constellation. In terms of operational benefits, a standard navigation receiver can carry through signal reception from all satellites within the field of view of its antenna, which enables a silent, low-cost operation with no additional contribution to electromagnetic pollution [17]. The receiver can be stationary or mounted on a surface vehicle or an aircraft.

The major scientific and engineering benefits in using GNSS as transmitter of opportunity lay in the structure of GNSS networks. GNSS constellations possess potential for permanent and continuous monitoring of the Earth's surface on a global scale. A fully operational GNSS constellation guarantees that any point on Earth is illuminated by several satellites (typically 6–8 for a single GNSS constellation) simultaneously from different angles, and therefore the satellites at the most appropriate positions could be selected for forming the optimal bistatic topology to achieve better spatial resolutions minimizing shadowing effects. Moreover, it also makes it possible to develop multi-static or multi-perspective SAR techniques [18].

The feasibility of the GNSS-based SAR technique has been theoretically and experimentally demon-

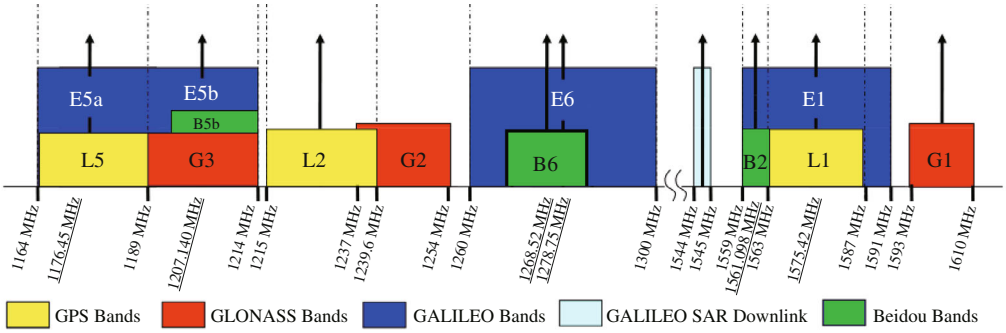

Figure 2 (Color online) GNSS navigation frequency bands [24] (China Satellite Navigation Office. BeiDou Navigation Satellite System Signal in Space Interface Control Document, Open Service Signal, 2013).

strated for both moving and stationary receivers [19,20], using Glonass [21] and Beidou [22], GPS [23] and Galileo [20] transmissions. This paper serves as a review on the scientific and engineering aspects of GNSS-based SAR. Section 2 overviews the GNSS resources, followed by the spatial resolution analysis and power budget evaluation for GNSS-based SAR in respectively Sections 3 and 4. In Section 5 the signal processing algorithms are reviewed, consisting of the synchronization and image formation. Following that in Section 6, several typical experimental results are presented as the verification. Next, advanced SAR techniques are discussed in Section 7, including coherent change detection (CCD), multi-perspective and multi-static imaging. Finally a conclusion is given in Section 8.

2 GNSS overview

Out of the four possible GNSS options, two of them are currently in full operation; these are the Global Positioning System (GPS) and the Global Orbiting Navigation Satellite System (GLONASS). The other two, Galileo and Beidou, are still on the deployment stage and scheduled to reach their full operational capacity in 2019 and 2020 respectively.

Navigation satellites continuously transmit navigation signals in two or more frequency bands within the L band. From the radar user's perspective, these signals contain ranging codes which can be used for remote sensing and also navigation codes. Figure 2 shows the GNSS frequency bands.

The GPS constellation consists of 24 satellites orbiting the earth in about 12 h, since the orbit altitude is 20180 km; the satellites repeat the same track and configuration approximately each 24 h (4 min earlier each day). There are six equally spaced (60° apart) orbital planes (nominally four space vehicles in each) and they are inclined at about 55° with respect to the equatorial plane.

The operational space segment of GLONASS consists of 21 satellites in 3 orbital planes, with 3 on-orbit spares. Each plane contains eight satellites identified by a "slot" number, which defines the corresponding orbital plane and the location within the plane: 1–8, 9–16, 17–24. The three orbital planes are separated by 120°, with the satellites equally spaced within the same orbital plane, being 45° apart. Each satellite operates in a circular 19130 km orbit (slightly lower than that of the GPS satellites) at an inclination angle of 64.8° and each satellite completes an orbit in approximately 11 h 15 min.

The full operational Beidou constellation is planned to be composed of 35 satellites, including 5 geostationary orbit satellites and also 30 medium Earth orbit satellites operating in six 21600 km-high orbits (slightly higher than that of the GPS satellites) at an inclination angle of 55° and each satellite completes an orbit in approximately 12 h.

When Galileo, Europe's own global satellite navigation system, is fully operational, there will be 30 new satellites in Medium Earth Orbit (MEO) around the earth at an altitude of 23222 km. 10 satellites will occupy each of three orbital planes inclined at an angle of 56° to the equator. The satellites will be spread equally around each plane and will take about 14 h to orbit the earth. At the moment 6 space vehicles in the constellation are in space, with more scheduled for launch.

3 Spatial resolution

The definition of bistatic target resolution is identical to that of monostatic target case: the degree to which two or more targets may be separated in one or more dimensions, such as angle, range, velocity (or Doppler) etc. In GNSS-based SAR systems, spatial resolution depends on the bistatic data collection geometry, where the optimal situation in terms of resolution is the quasi-monostatic case. A general method for bistatic SAR resolution analysis was proposed in [25], by means of the generalized ambiguity function (GAF) approach [26].

Figure 3 demonstrates the general bistatic SAR geometry for analysis. L denotes the bistatic baseline. $\boldsymbol{V}_T$, $\boldsymbol{\omega}_T$, $\boldsymbol{V}_T$ are the transmitter's velocity, angular speed and total angular movement respected to the target, while $\boldsymbol{V}_R$, $\boldsymbol{\omega}_R$, $\boldsymbol{A}_R$ are similar parameters of the receiver. $\boldsymbol{U}_T$, $\boldsymbol{U}_R$ represent the unit vectors from the transmitter and receiver to the target. Figure 4 gives the resolution projection on the ground plane for practical calculations, in which the cross-range dimension is also considered.

To obtain the resolution performance, we can refer to the point spread function (PSF) or GAF [2,25]. PSF describes the 2D correlation function of one point target and can be decomposed into the range and azimuth correlation functions, while the GAF is the 2D correlation function in the delay-Doppler domain. Therefore, the PSF and the GAF are representations of the same parameter but in different domains, and one can be transformed to the other via the appropriate domain transformation. The 3 dB widths of GAF in range and azimuth dimensions are respectively the range resolution and azimuth resolution. Considering a ground-based stationary receiver collecting the signals emitted from a GNSS transmitter and reflected by one stationary point target, the two-dimensional bistatic resolution cell of such a system can be derived from the GAF. In the hypothesis of narrowband signal and narrow synthetic aperture, GAF $|X(A,B)|$ is given by the product of two normalized functions, $p(\cdot)$ and $m_A(\cdot)$. The former is the matched filter output of the ranging signal and the latter is the inverse transform of the normalized received signal magnitude pattern:

$$|X(A,B)| \approx p\left[\frac{2\cos(\frac{\beta}{2})\Theta^{\mathrm{T}}(r)}{c}\right] \cdot m_A\left[\frac{2\omega_E \Xi^{\mathrm{T}}(r)}{\lambda}\right], \tag{1}$$

where A is the vector position of the desired point reflector to be evaluated, vector B is an arbitrary position of another reflector in the vicinity of A and $r = B - A$; β is the bistatic angle and Θ is a unit vector in the direction of its bisector; $\omega_E = \frac{|\boldsymbol{\omega}_T + \boldsymbol{\omega}_R|}{2}$ and Ξ are referred to as the equivalent angular speed and the equivalent motion direction (since a monostatic SAR moving in the direction Ξ with angular speed ω_E would exhibit similar Doppler-based resolution characteristics); c is the speed of light and λ the wavelength. The superscript 'T' denotes the transpose of a matrix.

Under the GNSS-based bistatic topology, the experimental PSF can be obtained after image formation algorithm, and one example was presented in Figure 11 of [28]. It shows that there is a nearly perfect correspondence with the theoretical expected PSF. Therefore, the theoretical equation (1) is a credible prediction for the following spatial resolution analysis.

Accordingly, the range resolution δ_r and azimuth resolution δ_a can be calculated. Detailed derivation can be found in [25], and a general result can be written as

$$\delta_r = \frac{\delta_\tau c}{2\cos(\beta/2)} = \frac{c}{2B\cos(\beta/2)}, \quad \delta_a = \frac{\delta_D \lambda}{2\omega_E} = \frac{\lambda}{2T_c\omega_E}. \tag{2}$$

Denoting Θ and Ξ as the unit vector of $(\boldsymbol{U}_T + \boldsymbol{U}_R)$ and the unit vector of $(\boldsymbol{\omega}_T + \boldsymbol{\omega}_R)$. Then range resolution and azimuth resolution directions would be along Θ and Ξ respectively.

It can be concluded that for a high altitude transmitter and low altitude receiver (most cases in GNSS-based SAR), the receiver dominates the azimuth resolution since the angular speed of the receiver to the target is much bigger due to closer range to target. If geostationary satellites used, the transmitter's angular speed is negligible respect to the ground target so that only the receiver motion is taken into account to generate aperture synthesis. The potential azimuth resolution for GNSS-Based SAR can be

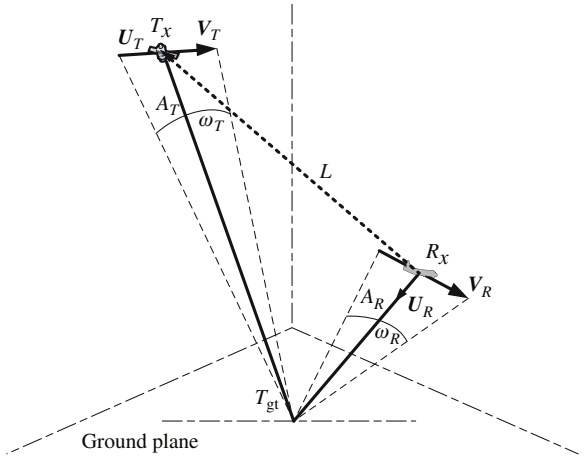

Figure 3 Bistatic SAR geometry and parameters definition [27].

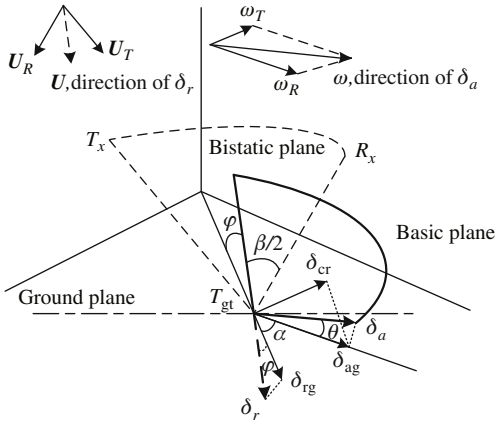

Figure 4 Resolution projection on the ground plane [27].

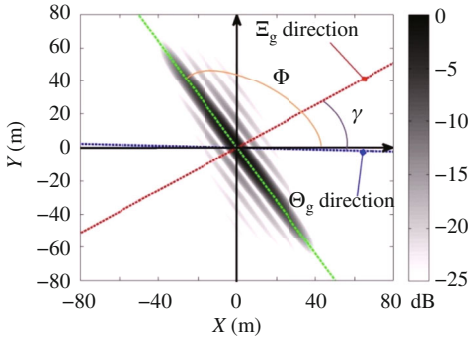

Figure 5 (Color online) Simulated GAF of GNSS-based SAR [18].

written as

$$\delta_a = \frac{\lambda R_R}{L_c} = \frac{\lambda R_R}{V_R T_c}, \tag{3}$$

where L_c is the length of the synthetic aperture.

Similarly, for the stationary receiver case, the synthetic aperture is generated only by the motion of satellite, and therefore the azimuth resolution can be calculated as

$$\delta_a = \frac{\lambda R_T}{V_T T_c}. \tag{4}$$

Most of the time, the resolutions projected on the ground have more practical meanings, and they can be calculated by

$$\delta_{\rm rg} = \frac{\delta_r}{\cos\varphi} = \frac{c}{2B\cos(\beta/2)\cos\varphi}, \quad \delta_{\rm ag} = \frac{\delta_a}{\cos\theta} = \frac{\lambda}{2T_c\omega_E\cos\theta}. \tag{5}$$

As an example, Figure 5 shows a simulated PSF for a scatterer in the scene centre and a GLONASS satellite (having a bandwidth of 5.11 MHz corresponding to a range resolution of 30 m under quasi-monostatic topology); β is about 71°and ω_E is 0.005°/s; the dwell time is 200 s (therefore a linear trajectory of the satellite can be assumed). The mutual positions of the receiver and the transmitter entail $\gamma \approx 34.2°$and the orientation of the resulting resolution ellipse is $\phi \approx 122°$. The resolutions in the range and azimuth directions projected onto the ground plane, $\delta_{\rm rg}$ and $\delta_{\rm ag}$ respectively, are defined along Θ_g and Ξ_g. However, the worst spatial resolution, $\delta_{\max}$, is along the major axis of the PSF while the best

one, $\delta_{\min}$, is along to minor axis of the PSF, being very close to Ξ_g. The parameters $\delta_{\min}$ and $\delta_{\max}$ will be used to characterize the spatial resolution capability of this system hereafter, since they represent its lower and upper bounds. In this example, the area of the resolution cell and the resolutions $\delta_{\max}$ and $\delta_{\min}$ are about 357 m^2, 76 m (while δ_{rg} is 44 m) and 4.7 m (slightly better than $\delta_{\mathrm{ag}} = 5.12$ m), respectively.

According to (2), the range resolution of the GNSS-based SAR depends only on the ranging code bandwidth and the bistatic geometry. For example, assuming a GLONASS transmitter, the transmitted P-code occupies a 5.11 MHz bandwidth, and therefore the corresponding range resolution under quasi-monostatic topology is around 30 m, which may further degraded by bistatic geometries. According to (4), for stationary receiver configuration, since the satellite-to-target range R_T and satellite's velocity V_T may not change a lot during the dwell time, the azimuth resolution depends mainly on the dwelling time. For all GNSS satellites, in order to achieve a sufficiently high azimuth resolution (less than 3 m), long dwell times on target are required, in the order of 5 min or higher. This dwell time is possible due to the extended area coverage of the satellite. However, over this interval, the satellite's trajectory cannot be approximated as a straight line. Apart from implications on image formation algorithms, which have been considered for monostatic SAR [29], the curved satellite trajectory also affects the resolution cell size and orientation that shape the system PSF. In [30], an extended GAF is derived for bistatic geometry with a curved satellite trajectory. Firstly the curved trajectory of the transmitter was written as

$$R_T(u) = R_T(u_C) + V_T(u - u_C) + \frac{1}{2}a_T(u - u_C)^2 + \cdots, \tag{6}$$

where u_C marks the midpoint of the synthetic aperture, and acceleration vector $\boldsymbol{a}_T$ accounts for the nonlinearity of the trajectory. The extended GAF has been found equal to

$$|X(A,B)| \approx \left| \int p\left[\frac{f_{\mathrm{dc}}}{f_c} \cdot (\bar{u})\right] \widetilde{M}_A(\bar{u}) \exp(\mathrm{j}2\pi f_{\mathrm{dc}}\bar{u} + \mathrm{j}\pi f_{\mathrm{dr}}\bar{u}^2)\mathrm{d}\bar{u} \right|, \tag{7}$$

where $\bar{u} = u - u_C$. f_c is the carrier frequency of the transmitted signal. f_{dc} is the Doppler centroid difference between two scatters and f_{dr} is the Doppler chip rate difference. They are given by

$$\begin{cases} f_{\mathrm{dc}} = \dfrac{1}{\lambda}(U_{\mathrm{TB}} - U_{\mathrm{TA}})^{\mathrm{T}} V_T, \\ f_{\mathrm{dr}} = \dfrac{1}{\lambda}\left\{(U_{\mathrm{TB}} - U_{\mathrm{TA}})^{\mathrm{T}} a_T + V_T^{\mathrm{T}}\left[\dfrac{I_{3\times 3} - U_{\mathrm{TB}}^{\mathrm{T}} U_{\mathrm{TB}}}{|B - R_T(u_C)|} - \dfrac{I_{3\times 3} - U_{\mathrm{TA}}^{\mathrm{T}} U_{\mathrm{TA}}}{|A - R_T(u_C)|}\right] V_T\right\}. \end{cases} \tag{8}$$

Comparing the performance of (1) and (7) for practical cases with different dwelling duration, experimental results (Figure 5 of [30]) verified the superiority of the extended GAF than the old formula.

With regard to the GNSS-based SAR with moving receiver configurations, the potential Doppler resolution corresponds approximately to the receiver antenna aperture that is twice less in comparison with the monostatic SAR. For the stationary receiver cases, the Doppler resolution is restricted by the satellite trajectory length visible from the receiver. It can be limited to 3–4 m in practical case by using long dwell times (typically 5–10 min) on target. The range resolution, similar to a traditional radar, is fully specified by the transmit signal bandwidth, but is further degraded by bistatic acquisition geometry. For example, in a quasi-monostatic configuration, using the GLONASS P-code (5.11 MHz) bandwidth, the range resolution is 30 m. While using Galileo E5a or E5b or GPS L5 signals, a bandwidth of 10.23 MHz can yield a quasi-monostatic resolution of 15 m as the best.

4 Power budget

The receiver records two signals via two separate channels. The heterodyne channel (HC) records the direct satellite-receiver signal for signal synchronization, while the radar channel (RC) records satellite signal reflections from an observation area for imaging. Therefore, to consider the power budget of GNSS-based SAR, we hereby at first discuss the transmitter parameters, including power output, equivalent isotropic radiated power (EIRP), etc., and then power budget would be analysed for the radar channel.

Table 1 Transmitter's parameters [27]

Transmitter	Power output (W)	EIRP (dBW)	Orbit altitude (km)	Power density (dBW/m^2)
Galileo	50	32	23222	−126
GPS	50	30	20180	−127
GLONASS	50	28	19130	−128

For power budget calculation, the first two parameters concerned are the power transmitted by the transmitter and the power available on or near the receiver or target area. In radio communication systems, EIRP is the amount of power that would have to be emitted by an isotropic antenna (that evenly distributes power in all directions and is a theoretical construct) to produce the peak power density observed in the direction of maximum antenna gain. EIRP can take into account the losses in transmission line and connectors and includes the gain of the antenna. The EIRP allows making comparisons between different transmitters regardless of type, size or form. From the EIRP, and with knowledge of a real antenna's gain, it is possible to calculate real power and field strength values.

$$\text{EIRP} = P_T - L_f + G_a, \tag{9}$$

where EIRP and P_T (power output of transmitter) are in dBm, cable losses (L_f) is in dB, and antenna gain (G_a) is expressed in dBi, relative to a (theoretical) isotropic reference antenna.

In general the EIRP coverage of GNSS signal produces the uniform power flux density on the earth's surface; however, this is not the case for most of broadcasting and communications satellite as well as GNSS. One can expect about 5-6 dB signal power difference between the satellite's antenna beam centre and the edge of the beam [27].

Table 1 shows the main parameters relating to signals radiated by three GNSS systems. The values are based on free space propagation and the global beam is considered. GPS, GLONASS and Galileo systems generate more or less same EIRP, while Galileo having 4 dB higher EIRP than GLONASS.

In [29], two types of configurations were considered, one uses airborne receiver (Figure 6(a)), while the other uses stationary receiver (Figure 6(b)). Assuming a quasi-monostatic case, the range resolution and azimuth resolution is calculated.

After the range and azimuth compression, the final system signal-to-noise ratio (SNR) is

$$\frac{S}{N} = \Pi_1 \cdot \frac{A_r \sigma}{4\pi R_R^2} \cdot \frac{1}{KT_0BF} \cdot \frac{\tau_i}{\tau_0} \cdot \frac{\text{PRF} \cdot R \cdot \lambda}{V\delta_a} \cdot \eta, \tag{10}$$

with $\Pi_1 = \frac{\text{EIRP}}{4\pi R_T^2}$ being the power flux density near Earth's surface produced by the GNSS transmitter. For a Galileo single channel, $\Pi_1 \approx 3.0628 \times 10^{-14}$ Wt/m^2 , while for other GNSS signals the power density is in the same order. τ_0 and τ_i are respectively the signal durations of compressed and uncompressed range signal, and the term (τ_i/τ_0) is the SNR gain after range compression, which for GNSS-based SAR is the correlation between the reflected and reference signals via the synchronization between the receiver and satellite. Likewise, the term $(\text{PRF}{\cdot}R\lambda/V\delta_a)$ is a number of integrated signals during the synthetic dwell time, which is the SNR gain after the azimuth compression. Assuming that the system loss factor is $\eta \approx 0.5$ and the receiver system noise bandwidth and the transmitting signal bandwidth are matched, so that $B \cdot \tau_0 = 1$ and we can take into account $\text{PRF}{\cdot}\tau_i = 1$. The noise coefficient of the receiver can be considered as 1 dB.

For airborne receiver configuration (Figure 6(a)), the SNR equation is

$$\frac{S}{N} = \frac{\Pi_1 A_r \sigma t_c \cdot \text{PRF} \cdot \lambda\eta}{4\pi R_R F_n K T_0 V_a \delta_a}, \tag{11}$$

where t_c is the period of transmitting signal code, and V_a is the airplane velocity. Based on this analysis, some results of the calculation are conducted and presented in Table 2.

For stationary receiver configuration (Figure 6(b)), the SNR equation is

$$\frac{S}{N} = \frac{\Pi_1 A_r R_T \lambda\eta}{4\pi F_n K T_0 \delta_a} \frac{\sigma}{R_R^2 V_s}, \tag{12}$$

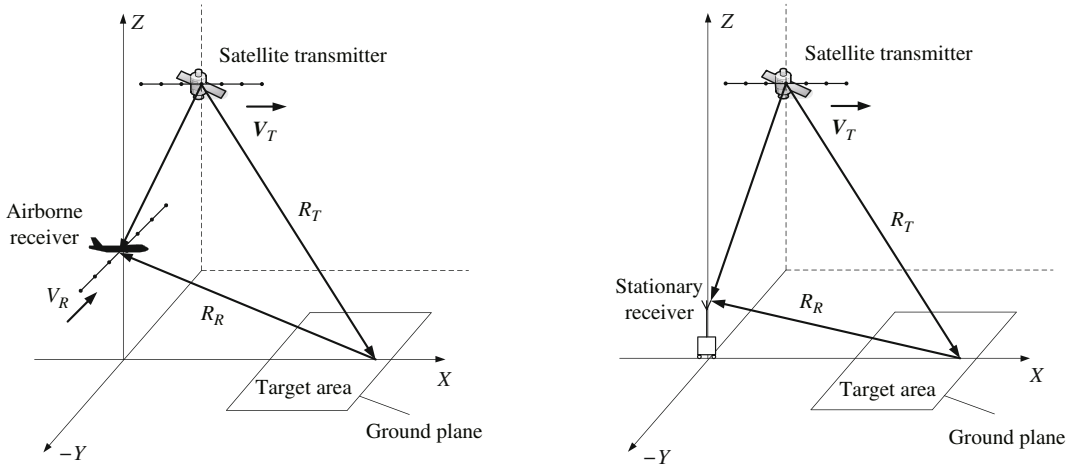

Figure 6 Two configurations of GNSS-based SAR system. (a) Airborne receiver system; (b) stationary receiver system [27].

Table 2 Power budget of GNSS-based SAR with airborne receiver [29]

RCS (m^2)	10	50	50	50	50	250	250
Distance receiver-target (km)	3	3	6	10	10	10	15
Receiver speed (m/s)	25 (90 km/h)	25	25	25	50 (180 km/h)	25	50
Integration time (s)	30.6	30.6	61.2	102	51	102	76.5
Signal-to-noise (power ratio-dB)	6.17	13.16	10.15	7.93	4.92	14.92	10.15

Table 3 Power budget of GNSS-based SAR with stationary receiver [29]

RCS (m^2)	1	1	10	10	50	50	250	250
Distance receiver-target (km)	1	2	3	10	10	30	15	30
Satellite speed (m/s)	3500	3500	3500	3500	3500	3500	3500	3500
Integration time (s)	1000	1000	1000	1000	1000	1000	1000	1000
Signal-to-noise (power ratio-dB)	20.86	14.84	21.32	10.86	17.85	8.31	21.32	15.29

with δ_a in accordance with (4). Based on this analysis, some results of calculations with different parameters σ and R_R are presented in Table 3.

The analysis introduced above does not include ways of further power budget improvement. SNR can be improved essentially by using non-coherent integration of signals from more than one transmitting channel, for example the Galileo E5 channels.

For the stationary receiver the power budget is more favorable owing to an essentially longer integration time. This system can be more attractive for interferometric observation [31], change detections [32], etc. in a regional area restricted by the horizon.

5 Signal processing

5.1 Synchronization of GNSS-based SAR

As the transmitter and receiver are spatially separated, signal synchronization is needed to maintain the coherence required for image formation. GNSS-based SAR receiver uses one channel (HC) to record the direct signal from the satellite for synchronisation, while another channel (RC) collects satellite signal reflections from an observation area for imaging. Both the HC and RC have the same clocks and local oscillators, and therefore they have the same clock slippage and local oscillator drift compared to the satellite. As a result, clock slippage and oscillator drift can be deducted through the delay and phase

tracking of the direct signal at the HC and then be used to compensate the corresponding delay and phase terms at the RC.

Even if the HC antenna is pointed towards the satellite to maximise the direct signal strength, the SNR at the input of the receiver can be as low as −40 dB, so a tracking algorithm based on matched filtering is required to maximise it. That way the direct signal delay and phase can be tracked and extracted from the clock slippage and oscillator drift. An additional problem we need to consider is the structure of all GNSS signals, Figure 1c of [33] shows a simplified modulation scheme of GLONASS signals transmitted in the L1 frequency band. The P-code and C/A code signals in different code rates are respectively the primary and secondary codes. Both the code sequences are added to 50 or 100 Hz navigation messages.

It is general that the GNSS signal consists of two ranging codes in the form of pseudo-random sequences generally (but not necessarily) modulating a navigation message. From these three sequences, only the primary ranging code is desired to yield the signal bandwidth for imaging, while the other two act as interference and are required to be cancelled in the algorithm The particular algorithm adapted from GNSS signal tracking to GNSS-based SAR synchronisation was the well-known Block Adjustment of Synchronising Signal (BASS) algorithm [33,34], but any GNSS tracking algorithm can fundamentally be adopted for this purpose. Its block diagram for signal synchronisation is shown in Figure 2 of [21].

As mentioned before, the signal required for SS-BSAR image formation is the primary code, and hence all of its parameters should be tracked for synchronisation. The BASS algorithm first tracks the secondary code parameters for its compensation in the following image formation, and then proceeds to track the required parameters of the primary code.

Matched filtering method (see Figure 3 of [21] for the block diagram) is involved to track the delay and coarse Doppler frequencies of the secondary code at every PRI, which for GNSS is usually 1ms, resulting in a pulse repetition frequency (PRF) of 1 kHz. Hence, this stage is a 2-D search algorithm in delay and Doppler, Figure 4 of [21] presents a typical 2-D delay/coarse frequency estimate for one PRI, obtained from experimental data. The location of the peak indicates the estimated delay and coarse frequency.

The following medium and fine frequency tracking steps can provide accurate Doppler value. Medium frequency tracking provides Doppler estimates with 200 Hz resolution through FFT processing, whereas fine frequency tracking operates on the phase difference between signals at adjacent PRIs. Based on all the tracked parameters of the secondary code, its corresponding component can be removed from the received signal. Besides, at the output of the fine frequency tracking, the direct signal Doppler has been estimated. The secondary code and primary code should share equal Doppler, since it is defined as the derivative of their phases.

After obtaining the signal with only the component of the primary code, matched filtering is used again to track the primary code delay and the signal phase. Finally, the primary code phase and the navigation message (if necessary) can be extracted according to the detected signal phase, as shown in Figure 6 of [21]. The navigation message is a BPSK signal, and can be regarded as a phase transition of the primary code phase. Therefore, using a phase transition detector, the navigation message and the primary code phase can be separated.

At the output of the signal synchronisation, the direct signal time delay, Doppler, phase and navigation message are tracked. The aforementioned algorithm has been validated by some experimental examples for a GLONASS transmitter and a fixed receiver (Figure 7) or an airborne receiver (Figure 8).

Figure 7(a) shows the tracked P-code delay in the direct signal, while Figure 7(b) presents the Doppler frequency at the output of the fine frequency tracker. In practice, a least-mean squares (LMS) algorithm is applied to the tracking output to smooth Doppler variation due to receiver noise. However, both delay and Doppler outputs are clear and without significant errors.

The tracked phase spectrum is shown in Figure 7(c). This result was generated by taking the complex exponential of the tracked phase, followed by an FFT. Effectively, this is the azimuth spectrum of the direct signal. The obtained results show a near-perfect chirp signal spectrum, which is as expected from the instantaneous phase history of the satellite. Finally, Figure 7(d) presents the decoded navigation message in the first 5 s of the data for better visualisation.

The results presented in Figure 7 demonstrate the functionality high performance level of the proposed

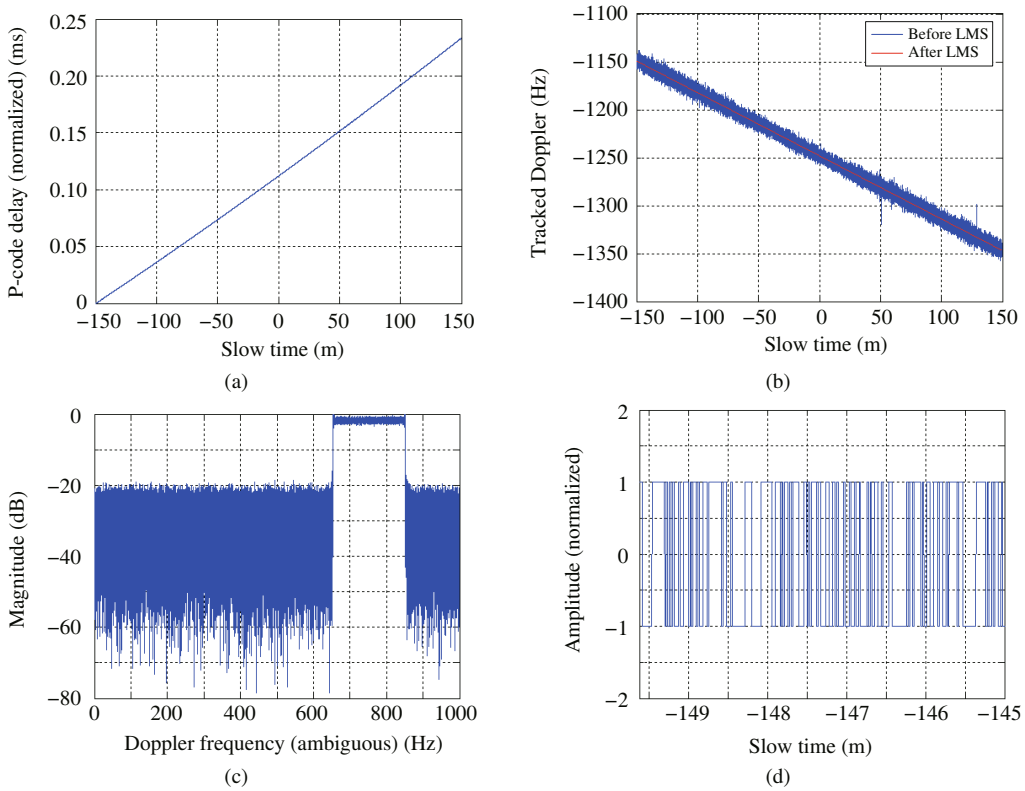

Figure 7 (Color online) Tracked direct signal parameters. (a) Delay, (b) Doppler, (c) phase spectrum, and (d) decoded navigation message [21].

method. Note that the tracked outputs contain the true time delay and Doppler variation, as well as receiver artifacts such as clock slippage and local oscillator drift.

In a manner similar to Figure 7, Figure 8 shows the tracked direct signal parameters obtained using a Galileo transmitter (E5b-Q signal) and an airborne receiver during flight.

Comparing Figure 8 and Figure 7, it is clear that the direct signal Doppler in the moving receiver case is influenced by the trajectory deviations of the helicopter during its flight. The same effect is also visible in the tracked azimuth phase spectrum, which is no longer representative of a chirp signal (Figure 8(c)).

A number of conclusions can be derived from the experimental results. First, the proposed algorithm can operate irrespective of the selected GNSS transmitter, and irrespective of the topology, even in a dynamic environment where the airplane trajectory deviations affect the direct signal parameters. In terms of the performance, all tracked outputs are obtained with sufficiently high signal-to-noise ratios (SNR). In the fixed receiver case, the tracked Doppler curve is linear, implying a stable signal Doppler history that resembles a chirp signal. In the moving receiver case, effects of trajectory deviations are visible, an issue which should be dealt with at the image formation stage.

5.2 Image formation

Following signal synchronisation, an image formation algorithm is required to generate imagery of an interrogated scene. In the general BSAR case, image formation algorithms need to take two things into account. The first is the outputs of the synchronisation algorithm to maintain coherence, and the second is the topology of the bistatic acquisition. The reason for the latter is that different acquisition geometries imply different bistatic range/Doppler histories, which may or may not allow efficient processing algorithms in the frequency domain. This is particularly true for the SS-BSAR case, where there is little control in the choice of acquisition geometry due to the space-borne transmitter. Another factor to consider is the receiver configuration. A fixed receiver on the ground may be generally simpler in terms

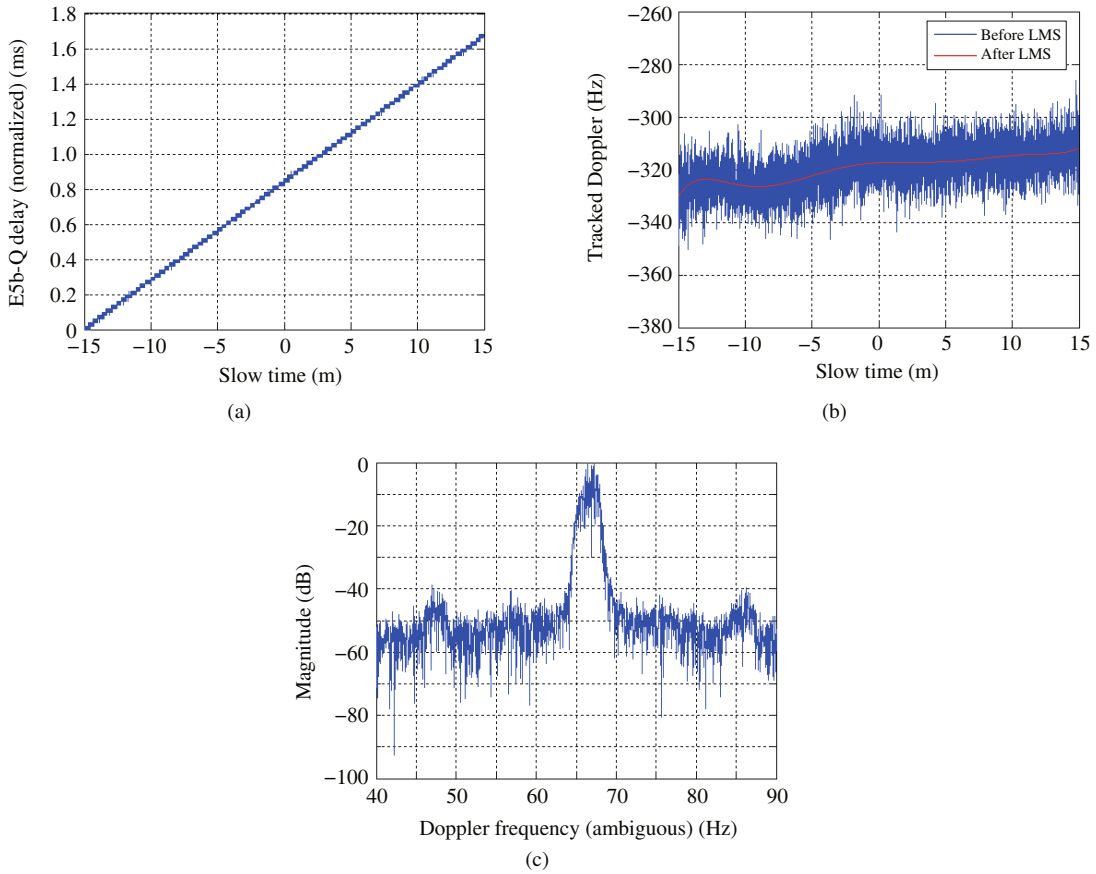

Figure 8 (Color online) Tracked direct signal parameters. (a) Delay, (b) Doppler, and (c) phase spectrum [21].

of the processing, however it would require essentially longer dwell times on target for a sufficiently high azimuth resolution, over which the satellite's trajectory cannot be approximated as linear and frequency-based algorithms are difficult to derive. On the other hand, a moving receiver has the added complexity of motion compensation.

It is for these reasons that perhaps the most universal solution for GNSS-based SAR is the use of a Back-Projection Algorithm (BPA) for image formation. It is not as efficient as a frequency-based algorithm, however it can treat non-linear satellite trajectories for fixed receiver cases as well as motion compensation (MoComp) for moving receivers, if needed. The concept of the BPA is the same as in the monostatic SAR case and its block diagram is shown in Figure 11 of [21], followed by a qualitative explanation of each block.

Two major steps are required to achieve the image formation: the range compression and the back-projection integral calculation. For the GNSS-based SAR case, the reference signal for range compression is generated based on the parameters obtained by synchronization, during which the delay and the phase are tracked both including errors of t_e and φ_e. Since these errors equal to both HC and RC channels, in order to compensate for receiver and atmospheric errors, they are separated from the corresponding signal parameters which can be calculated precisely and removed from the synchronization outputs if the transmitter and receiver positions during the time of acquisition are known. The accurate satellite position history corresponding to the data acquisition time can be obtained from the international GNSS service official website [35].

Range compression can be conducted in the fast-time frequency. Here, the reference signal is generated according to the synchronization results to cancel out delay and phase artifacts due to atmospheric and receiver errors. At the output of this operation, the range-compressed RC data is the cross-correlation function between the received and reference signals, and the time delay and phase histories of each target

depend on the radio wave propagation path, as dictated from the transmitter and receiver positions at the time of measurement. Following that operation, the computation of the back-projection integral may be performed in a similar manner to the monostatic case, but taking into account the bistatic target time delay rather than the monostatic round trip delay [36]. For the moving receiver case, it is straightforward to integrate a MoComp process to the back-projection integral computation for each image pixel, and the accuracy of this scheme relies on the accurate knowledge of the receiver positions [20], as in the monostatic case.

It is worth noting here that the BPA is not the only option for GNSS-based SAR imaging, and research has been done on more complex, but more computationally efficient algorithms for this purpose. For example, a range migration algorithm has been developed in [37] for GNSS-based SAR with a fixed receiver, as well as a modified range-Doppler algorithm for both the fixed and moving receiver cases [38].

6 Experimental results

The signal processing algorithms described in the last section have been applied to experimental data collected both from fixed and moving receivers. The aim of this section is to demonstrate experimental imagery obtained from these configurations. These images confirm not only the functionality of the algorithms employed, but also the feasibility of each system.

6.1 GNSS-based SAR experiment with stationary receiver

A series of experimental data sets were collected using GLONASS transmitters and a fixed receiver. For knowledge of the transmitter and receiver positions, the receiver location in the experiment was marked using a standard GPS receiver and precise satellite ephemeris data were acquired (5 cm accuracy). Satellite positions were given at a 15 min interval in the WGS84 co-ordinate system. To conform to the PRF of 1 kHz, these data were interpolated using a 10th order Lagrange polynomial. Then the co-ordinates of the transmitter and receiver were converted from WGS84 to a local co-ordinate system with the location of the HC as the origin.

The receiver was placed at the 35 m-high roof of the School of Electronic, Electrical and System Engineering (EESE) of the University of Birmingham. The RC antenna was overlooking the area to the west of the building. A satellite photograph taken from Google Earth of the observation area is shown in Figure 9. There are two areas of characteristic. First are four isolated towers approximately 1.2 km away from the receiver, which could serve as reference targets. Secondly are tree lines facing towards the receiver and yielding high strength echoes. The experimental radar images, after signal synchronisation and image formation are superimposed on the photograph in Figure 9 and presented in Figure 10. Figure 10 shows a good coincidence between the radar image and the satellite photograph. The locations of areas with buildings correspond to areas of high echo intensity in the image, while grassy areas exhibit a low reflectivity.

6.2 GNSS-based SAR experiment with moving receiver

The experimental data set was collected using Galileo as the transmitter, while the receiver was mounted on a ground moving vehicle (Figure 14 of [21]). Trials were taken in the area of Cleehill, Ludlow, UK [20]. The experimental parameters are shown in Table 4 of [21]. The experimental site and the radar image are shown in Figure 11. Note that the elevation of the receiver was comparable to the imaging scene, and therefore the majority of signal returns were collected from the front face of the buildings.

The observation area consists of four sparsely separated buildings which should be readily visible in the radar image. All four targets have been detected. Additionally, lower intensity echoes match to the orientation of tree lines in the photograph. To verify this image, cross-sections in the area around Target 1 were taken along the range and cross-range directions (Figure 16 of [21]). The expected bistatic resolutions are 27 m in range and 1 m in cross-range.

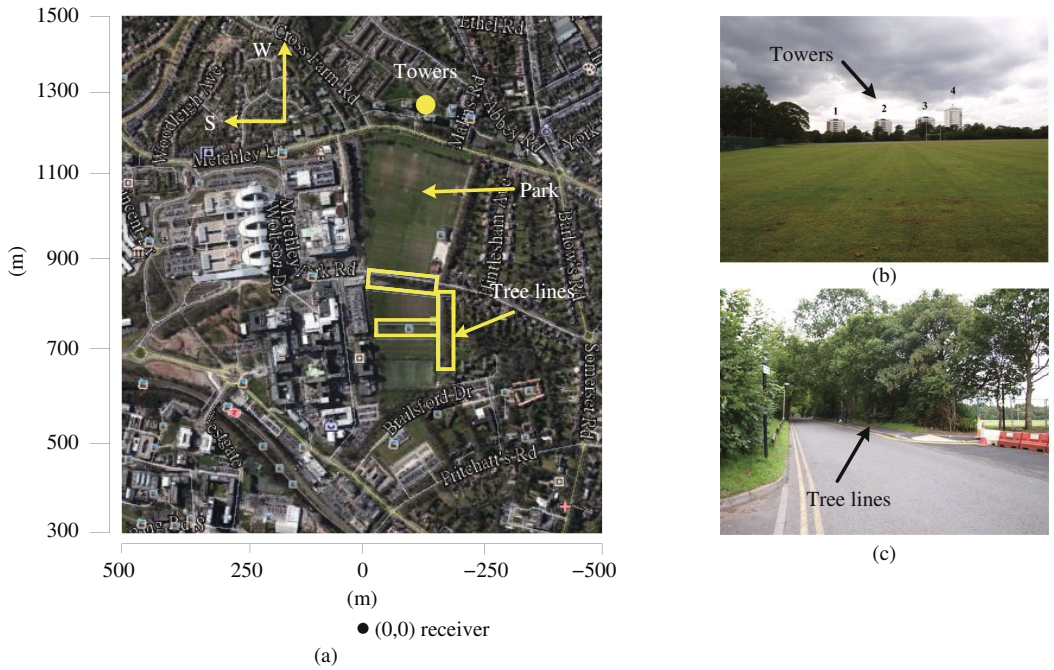

Figure 9 (Color online) Target scene. (a) Google Earth photograph of the target area; (b) and (c) optical photographs of two targets of concern [39].

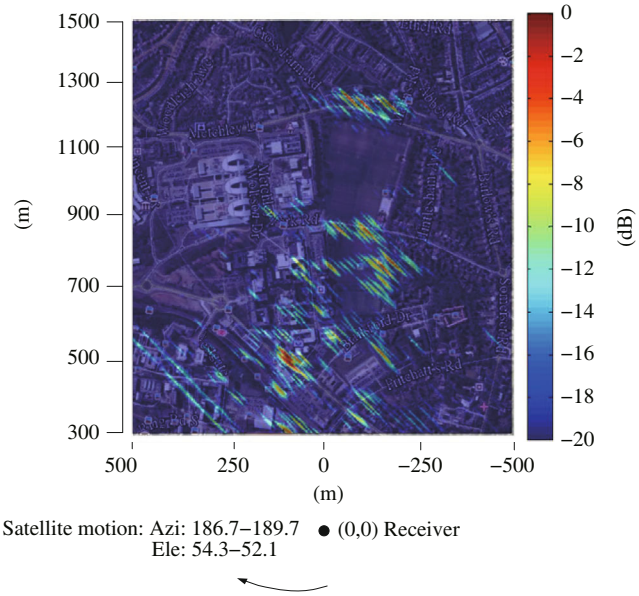

Figure 10 (Color online) Radar image super-imposed on imaging scene.

The width of the response of the target in range is 25.2 m, which is close to the expected range resolution. The theoretically predicted azimuth resolution is approximately 1 m, which is much smaller than the width of the building. However, the overall length of the target's response and its physical width can be compared. The total width of the target's response is approximately 22 m, in good accordance to its physical size. The smaller peaks on either side of the peak target response (the 0 dB point) are also noteworthy. They resemble the sidelobes of a sinc function, which is the form of the expected azimuth signal response. The magnitude of the rightmost peak is also approximately −12 dB. The magnitude of the leftmost peak is lower, at around −16 dB. This could be and image artifact due to inaccuracy in knowledge of the receiver's precise trajectory and velocity. However, both the range and azimuth cross-section analyses indicate proper system functionality.

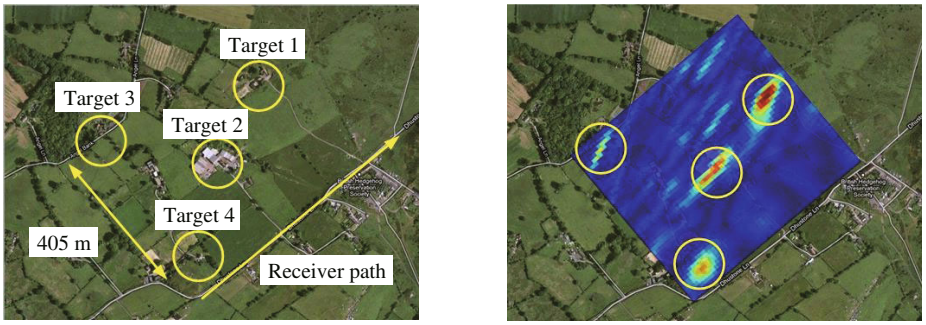

(a) (b)

Figure 11 (Color online) (a) Satellite photograph of imaging area (from Google Earth), and (b) radar image superimposed on imaging scene [21].

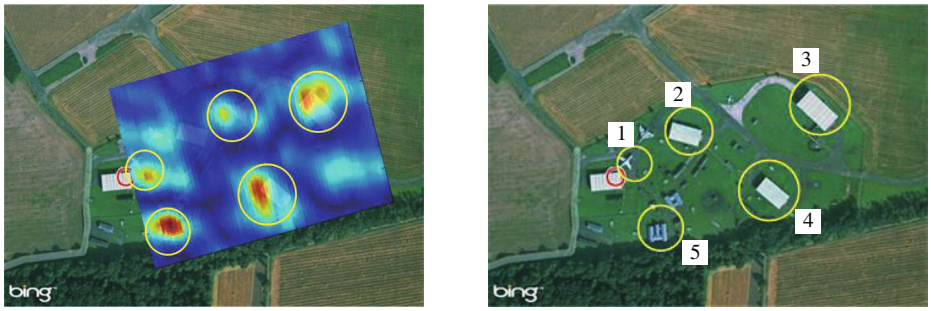

(a) (b)

Figure 12 (Color online) (a) Satellite photograph of imaging area, and (b) radar image super-imposed on imaging scene [21].

The other set of moving receiver measurements was taken using Galileo as the transmitter, while the receiver was mounted on an AS355 helicopter (Figure 17(a) of [21]). The same receiving hardware as in the ground moving vehicle case was used. Trials were done around the East Fortune airfield in Scotland (Figure 17(b) of [21]).

This set of data required MoComp processing due to the irregular motion of the helicopter, which was made worse by weather conditions at the time of measurement. This can be readily seen from the synchronisation results for this data set (Figure 8). The helicopter location was recorded with a standard GPS positioner with a 1 Hz update rate, which was not sufficient to sample trajectory deviations. Additionally, the helicopter was not equipped with any Inertial Navigation System (INS) and used its own GPS receiver to navigate. For these reasons, it was expected that the obtained imagery would not be as accurate as the previous two cases. The obtained image is shown in Figure 12, superimposed on a satellite photograph of the observed area.

The image shows that despite severe defocus, five main targets have been detected. All of them correspond to buildings (such as hangars) or aircraft which could yield significantly high reflections, such as Targets 4 and 5. Higher intensity parts in the lower right part of the image are due to an occupied car park.

It is clear from the observed imagery that the image is de-focused. For example, the signal return of an aircraft above the leftmost hangar (Target 1) appears to be completely smeared. Additionally, signal returns are not registered in their appropriate locations, such as Targets 2 and 4 (aircraft hangars) which appear shifted. Furthermore, Target 3 appears as multiple peaks in the image, implying asymmetric sidelobe levels in the point spread function. These artifacts are due to the accuracy and update rate of the GPS receiver onboard the helicopter, as well as the absence of any inertial navigation equipment on it, hence the inadequacy to sample trajectory deviations sufficiently. Nevertheless, the detected targets prove that such a system is feasible.

7 Advanced SAR techniques

The validation of the GNSS-based SAR capability has paved the way for the consideration of advanced SAR techniques. All of them are now at the proof of concept level, however the obtained results have so far shown clear potential and they are included in the following sections.

7.1 Coherent change detection

The GNSS-based SAR is intended for coherent change detection (CCD) applications in local landscapes. Clearly, GNSS are outmatched by imaging radar satellites in terms of radar performance, such as resolution and power budget. However, there are also reasons to support such a topology for this particular application. A single GLONASS or Galileo satellite has revisit cycles on the order of eight to nine days, which is already faster than most radar satellites for repeat-pass imagery. However, by considering multiple GNSS satellites, an "effective" revisit cycle can be formed that is not bound by a single satellite's orbital properties. For example, if eight to nine different satellites are used in daily sequence, the effective revisit cycle for repeat-pass imagery is one day and so on. Also, GNSS satellites transmit in L-band, which is within current trends for Earth observation, and have reasonable resolution cell sizes for these applications [28,40].

On the other hand, the development of such a technology is a major technical challenge. The literature for CCD in monostatic SAR is vast (the reader is prompted to [41–43] for some of the seminal papers on this topic). However, CCD has been considered little, if at all, for BSAR in general, let alone a passive BSAR with transmitters which are not radar satellites. For these reasons, a systematic study on the feasibility of such a system is required.

After the theoretical radar performance calculations and the experimental verification of the imaging capability of this system, the next step is the study on its potential for CCD. The CCD scheme proposed as a first stage is the coherence estimation of repeat-pass image pairs, as in the monostatic case. That is, consecutive images obtained at the revisit cycle of a single satellite will be compared at the phase level, and image decorrelation will be translated into actual surface change.

Nevertheless, due to the complexity of the system, it is required that some of its major aspects should be examined prior to a further system investigation, to decide whether it may be fundamentally feasible. An initial experimental programme of the system's capacity as a change detector is designed to verify its feasibility on the fundamental 'proof of concept' level. To prove this concept, an experimental programme was built (Figure 2 of [28]), using a low-gain antenna for the RC acting a semi-active transponder whose height was varied between consecutive satellite passes to emulate a surface change on the point target level. A total of 11 data acquisitions (Figure 3 of [28]) were made at the revisit cycle of a single GLONASS satellite. The processing flow chart for CCD was presented in Figure 4 of [28]. Selecting one set of data as master, the others can be considered as slaves. In conceptual terms, the trajectory of the slave is shifted progressively in time by the PRI and subtracted from the master (Figure 5 of [28]).

A pictorial comparison between the theoretical and experimental results is shown in Figure 13 of [28]. From the experimental results, the minimum and maximum displacement errors are 0.22 and 1.47 cm, respectively. The average error is calculated to be -0.4 cm, with a standard deviation of 1.15 cm. This is expected as the averaging process partially compensates phase errors. Nevertheless, even in the presence of cable phase noise, the CCD accuracy is high enough.

The results demonstrated above indicate that the proposed system yields sufficiently high stability and accuracy, even in the presence of artifacts due to the temperature sensitivity of the cable. It should be highlighted that, even though the results obtained are affected by factors out of control of the operational system, they are still viewed as the ideal performance measures which may not be reached in practice, since they were obtained under idealized conditions.

Since the above analysis and results have provided the proof of concept for the CCD technology, the full feasibility study was initiated. Hence, spatial decorrelation between repeat-pass GNSS-based SAR images was investigated. This study is needed in the development of this system to monitor temporal changes in a scene. The main challenge is that, in the BSAR configuration, spatial coherence depends on

the bistatic geometry. The theoretical framework to describe spatial coherence for this case was developed by extending well-established monostatic models [44]. In its analysis, theoretical results were initially supported by Monte Carlo simulations. To validate that theoretical model, the experimental image in Figure 12(b) of [44] was used and a 'master and slave images scheme' in Figure 13 of [44] was applied for the spatial decorrelation measurement. A master image was generated using data from the start time of acquisition and for a dwell time $T_{\rm sys}$ that was less than the dwell time T on target. Then a set of slave images was generated, with the same $T_{\rm sys}$ but starting N seconds later than the master image, with N from 1 to 30 s. In other words, N was the temporal separation between images, and then coherent maps were obtained and shown in Figure 15 of [44].

To compare experimental spatial decorrelation results with theoretical ones, two representative areas within the image were selected. The first one a single building yielding a strong compressed echo (Figure 16(a) of [44]). The second one contains a patch of trees (Figure 16(b) of [44]), which were also detected with a sufficiently high signal-to-noise ratio (SNR). The measured coherence plots were shown in Figure 17 of [44]. For comparison, the corresponding theoretical coherence values were calculated based on (13) and the experimental parameters and were plotted on the same graph. Averaging windows were used for the evaluation of the experimental curves in Figure 17 of [44].

The result shows that the experimentally obtained spatial coherence is consistent with the theoretical predictions made using the model developed in this paper, confirming its validity. It also shows that, in GNSS-based SAR, spatial decorrelation effects are not as dramatic as in the traditional spaceborne SAR cases and can be further minimized by choosing the appropriate satellite trajectories for change detection. In this example, even a time offset of 15 s between repeat passes leads to a spatial coherence higher than 0.9. There are some deviations between the theoretical and practical results, which may be attributed to the complexity of the target structures and the experiment itself. Even so, these deviations appear at temporal image separations (10 s or longer) which are not expected in practice.

7.2 Multi-perspective imaging

By selecting different bistatic topologies, diverse scattering effects can be seen for the same scene objects, when viewed from different angles. This multi-perspective technique can be potentially used to increase the amount of information of a given scene, and therefore more scene features may be indicated.

Accordingly, four GNSS-based SAR experiments were conducted with GLONASS transmitter and a fixed receiver, the experimental setup and target area (Figure 9) was as mentioned in previous chapters. The satellite positions during experiments were given in Figure 4 of [39]. The four experimental radar images, after signal synchronisation and image formation were superimposed on the imaging scene and presented in Figure 5 of [39].

Each image was obtained with a different bistatic configuration, and therefore resolution cell sizes and orientations varied between images. The results provide the potential that the spatial resolution limited by the ranging code can be improved by combining different bistatic images, which improves the entire SNR simultaneously. This potential should be firstly proved in the PSF level [18].

The images in Figure 5 of [39] can either be treated individually, or they can be combined (non-coherently or coherently) to increase area information. We will also discuss the specific multi-static technique in next sections.

In [22], BeiDou-2 was firstly chosen as transmitter of opportunity to construct a SSBSAR system, and to address the issue of synchronization, the authors proposed an approach based on error cancellation and navigation information extraction. Experiment was conducted and SSBSAR image with Beidou-2 as illuminator was firstly obtained. As Figure 13 shows, the result is abundant and scatters like trees, lawn, lake, road and even small isolated architectures like a series of gloriettes can be distinguished.

As the GNSS constellation is composed of many satellites, and each satellite has short revisit time, it is possible to utilize several satellites in different observing angles to form a multi-angle observation system. In [45], twenty-six BiSAR experiments were conducted in different configurations, and the scattering characteristics of these imaging results are analyzed. Based on a region-based fusion algorithm using

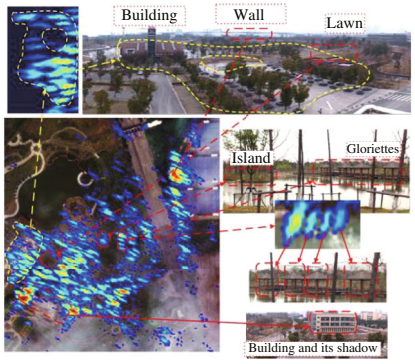

Figure 13 (Color online) SS-BiSAR image using BeiDou-2 as transmitter [22].

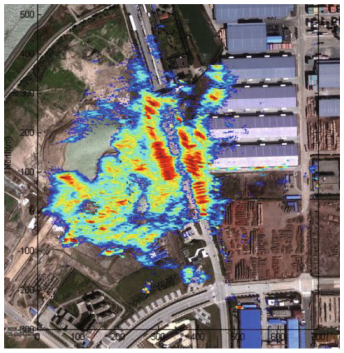

Figure 14 (Color online) SS-BiSAR multi-angle fusion image [45].

region of interest segmentation, a multi-angle fusion image was obtained as Figure 14 shows, which has many advantages, such as generating profiles, reconstructing shapes and enhancing details.

7.3 Multi-static imaging for spatial resolution improvement

From Figure 5 of [39], Each image was obtained with a different bistatic configuration, and therefore resolution cell sizes and orientations varied between images. The results provide the potential that the spatial resolution limited by the ranging code can be improved by combining different bistatic images, which improves the entire SNR simultaneously. This potential should be firstly proved in the PSF level, and therefore in [18] the Multistatic PSF (MPSF) was analytically derived by combining an arbitrary number of bistatic PSFs.

The idea is that different satellite positions and trajectories result in different bistatic PSF parameters: the bistatic PSF of No.n follows the format in (1) is characterized by specific directions of range and azimuth resolutions and different values of the bistatic angle and the equivalent angular speed as shown in (2). Therefore, a non-coherent combination of the individual PSFs, with their different orientations, results in a multi-static PSF whose resolution cell area is the overlapping segment of the single bistatic PSFs, and therefore may be essentially reduced. While considering the non-coherent addition method as a linear operation, the MPSF of $N \geqslant 2$ PSFs is:

$$\text{MPSF}: \frac{1}{N}\sum_{n=1}^{N} p\left(\frac{2\cos(\beta_n/2)\Theta_n^{\mathrm{T}}(r)}{c}\right)\cdot m_A\left(\frac{2\omega_{E_n}\Xi_n^{\mathrm{T}}(r)}{\lambda}\right), \tag{13}$$

with similar definitions of Θ_n, Ξ_n, β_n and ω_{E_n} as mentioned in (1) and Figure 5.

Similar combination strategies have been considered in the past for obtaining a multistatic radar system with improved performance; in [46] it has been proved that different performance optimization criteria lead to different weightings of the several bistatic links. However, here we equally weight all the bistatic links, assuming a calibration step already performed so that all the bistatic channels can be considered affected by the same free space attenuation.

One of the features of the single channel PSF represented by the GAF in (1) is that it is given by the product of two functions separately pertaining to the range and Doppler domain: even if the range and Doppler directions are not orthogonal their domains are still separable. For the MPSF in (13) this cannot be done since the summation and the modulus operator. But it can be approximated as [18]

$$\text{MPSF} \approx \bar{p}\bar{m}, \tag{14}$$

with $\bar{p}$ and $\bar{m}$ being

$$\bar{p} = \frac{1}{N}\sum_{m=1}^{N} p_n = \frac{1}{N}\sum_{m=1}^{N} p\left(\frac{2\cos(\beta_n/2)\Theta_n^{\mathrm{T}}(r)}{c}\right), \quad \bar{m} = \frac{1}{N}\sum_{m=1}^{N} m_{A_n} = \frac{1}{N}\sum_{m=1}^{N} m_A\left(\frac{2\omega_{E_n}\Xi_n^{\mathrm{T}}(r)}{\lambda}\right). \tag{15}$$

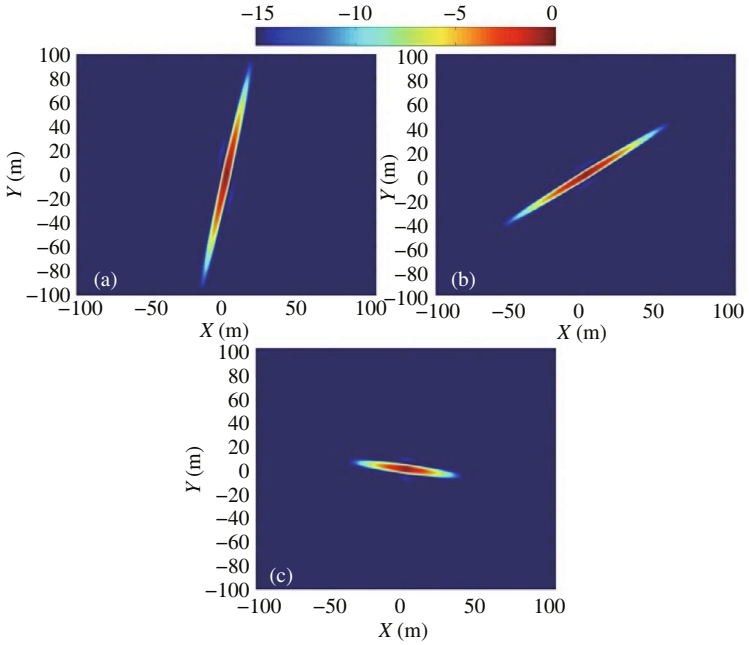

Figure 15 (Color online) Simulated bistatic PSFs. (a) A1, (b) A2, and (c) A3 [18].

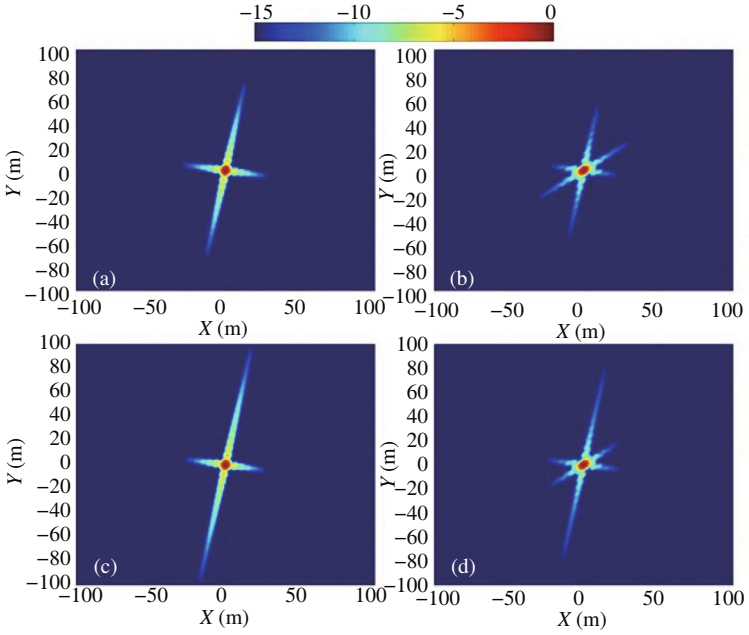

Figure 16 (Color online) Simulated multistatic PSFs and approximated version. (a) A1+A3, (b) A1+A2+A3, (c) A1+A3 (approximated), and (d) A1+A2+A3 (approximated) [18].

In this expression the range and Doppler domains are again separated. This approximation can be easily proven setting $p_n \approx p$, true in a wide zone around the mainlobe of the MPSF: since each $p_n(\cdot)$ function has a very wide mainlobe, due to the bistatic geometry, the limited bandwidth and the elevation angle of the satellite [2], the differences between the several $p_n(\cdot)$ can be assumed negligible, despite their different orientations.

The parameters of the bistatic PSFs are shown in Figure 15, and Figure 16 gives the MPSF achieved by combining two bistatic channels (A1 and A3, Figure 16(a)).

Comparing the bistatic PSFs in Figure 15 and the MPSFs in Figure 16, the reduction of the resolution cell area compared to the single PSFs is evident for $N = 2$. Increasing the number of combined channels,

the main effect is the reduction of sidelobe levels around the peak, while the mainlobe region remains approximately the same as the one achieved by integrating two channels, as long as the transmitters positions entail different PSFs orientations. An improvement of the worst spatial resolution is achieved, and as a consequence a reduction of the resolution cell area of about five times can be seen between the bistatic and multistatic cases. Figure 16 (c) and (d) show the approximated version of the MPSF achieved from (14) for the same cases in Figure 16(a) (A1+A3) and Figure 16(b) (A1+A2+A3). A good agreement between the nominal and the approximated version of the MPSF can be observed, particularly around the mainlobe. As a further verification, the experimental MPSF attempt was shown in Figure 8(e) of [18], with a good coincidence with the simulated expectations (Figure 8(f) of [18]).

8 Conclusion

This paper reviews the development of GNSS-based SAR and its derivative advanced techniques. A few conclusions can be made. First of all, this passive SAR technique and its available resources have been analysed and multiply verified by experimental results under different receiver configurations and different bistatic topologies. Second, a main problem revealed is the range resolution limitations of this system, but it may be tackled by the aforementioned multi-static scheme or a wider band signal of the forth coming satellites. Finally, the paper also indicates new potentials using this technology, such as CCD for observations of purpose and multi-static technique for multiple information detections.

References

1 Willis N J. Bistatic Radar. Boston: Artech House, 1991
2 Cherniakov M. Bistatic Radars: Emerging Technology. Hoboken: Wiley, 2008
3 Moccia A, Chiacchio N, Capone A. Spaceborne bistatic synthetic aperture radar for remote sensing applications. Int J Remote Sens, 2000, 21: 3395–3414
4 Walterscheid I, Espeter T, Brenner A R, et al. Bistatic SAR experiments with PAMIR and TerraSAR-Xsetup, processing, and image results. IEEE Trans Geosci Remote Sens, 2010, 48: 3268–3279
5 Rodriguez-Cassola M, Baumgartner S V, Krieger G, et al. Bistatic TerraSAR-X/F-SAR spaceborneCairborne SAR experiment: description, data processing, and results. IEEE Trans Geosci Remote Sens, 2010, 48: 781–794
6 Martinsek D, Goldstein R. Bistatic radar experiment. In: Proceedings of European Conference on Synthetic Aperture Radar (EUSAR), Friedrichshafen, 1998. 31–34
7 Walterscheid I, Ender J H G, Loffeld O. Bistatic image processing for a hybrid SAR experiment between TerraSAR-X and PAMIR. In: Proceedings of IEEE International Conference on Geoscience and Remote Sensing Symposium (IGARSS), Denver, 2006. 1934–1937
8 Wang R, Loffeld O, Nies H. Focusing results and analysis of advanced bistatic SAR experiments in spaceborne or airborne/airborne or stationary configurations. In: Proceedings of European Conference on Synthetic Aperture Radar (EUSAR), Aachen, 2010. 1–4
9 Behner F, Reuter S. HITCHHIKER-hybrid bistatic high resolution SAR experiment using a stationary receiver and TerraSAR-X transmitter. In: Proceedings of European Conference on Synthetic Aperture Radar (EUSAR), Aachen, 2010. 1–4
10 Zeng T, Hu C, Wu L, et al. Extended NLCS algorithm of BiSAR systems with a squinted transmitter and a fixed receiver: theory and experimental confirmation. IEEE Trans Geosci Remote Sens, 2013, 51: 5019–5030
11 Zeng T, Wang R, Li F, et al. A modified nonlinear chirp scaling algorithm for spaceborne/stationary bistatic SAR based on series reversion. IEEE Trans Geosci Remote Sens, 2013, 51: 3108–3118
12 Cristallini D, Caruso M, Falcone P, et al. Space-based passive radar enabled by the new generation of geostationary broadcast satellites. In: Proceedings of IEEE Aerospace Conference, Big Sky, 2010. 1–11
13 Cherniakov M, Nezlin D, Kubik K. Air target detection via bistatic radar based on LEOS communication signals. IEE Proc Radar Sonar Navig, 2002, 149: 33–38
14 Griffiths H, Baker C J, Baubert J, et al. Bistatic radar using satellite-borne illuminators. In: Proceedings of RADAR 2002, Edinburgh, 2002. 1–5
15 Tan D, Sun H, Lu Y, et al. Passive radar using global system for mobile communication signal: theory, implementation and measurements. IEE Proc Radar Sonar Navig, 2005, 152: 116–123
16 Cherniakov M, Saini R, Zuo R, et al. Space surface bistatic SAR with space-borne non-cooperative transmitters. In: Proceedings of European Radar Conference, Paris, 2005. 9–12
17 Cherniakov M. Space-surface bistatic synthetic aperture radar-prospective and problems. In: Proceedings of Proceeding of RADAR 2002, Edinburgh, 2002. 22–25
18 Santi F, Antoniou M, Pastina D. Point Spread Function Analysis for GNSS-Based Multistatic SAR. IEEE Geosci Remote Sens Lett, 2015, 12: 304–308

19 Antoniou M, Zeng Z, Liu F F, et al. Experimental demonstration of passive BSAR imaging using navigation satellites and a fixed receiver. IEEE Geosci Remote Sens Lett, 2011, 9: 477–481
20 Antoniou M, Zhou Z, Zeng Z, et al. Passive bistatic synthetic aperture radar imaging with Galileo transmitters and a moving receiver: experimental demonstration. IET Radar Sonar Navig, 2013, 7: 985–993
21 Antoniou M, Cherniakov M. GNSS-based bistatic SAR: a signal processing view. EURASIP J Adv Signal Process, 2013. 1–16
22 Tian W, Zhang T, Zeng T, et al. Multi-angle fusion of SS-Bi SAR images using Compass-2/Beidou-2 satellites as opportunity illuminators. In: Proceedings of IEEE International Conference on Radar, Lille, 2014. 1–4
23 Maussang F, Daout F, Ginolhac G. GPS ISAR passive system characterization using point spread function. In: Proceedings of New Trends for Environmental Monitoring Using Passive Systems, Hyeres, 2008. 1–4
24 Subirana J S, Zornoza J J, Pajares M H. GNSS signal. Navipedia, 2011
25 Zeng T, Cherniakov M, Long T. Generalized approach to resolution analysis in BSAR. IEEE Trans Geosci Remote Sens, 2005, 41: 461–474
26 Cherniakov M, Zeng T, Plakidis E. Ambiguity function for bistatic SAR and its application in SS-BSAR performance analysis. In: Proceedings of the International Radar Conference, Adelaide, 2003. 343–348
27 Zuo R. Bistatic synthetic aperture radar using GNSS as transmitters of opportunity. Dissertation for the Doctoral Degree. Birmingham: University of Birmingham, 2012
28 Liu F, Antoniou M, Zeng Z, et al. Coherent change detection using passive GNSS-Based BSAR: experimental proof of concept. IEEE Trans Geosci Remote Sens, 2013, 51: 4544–4555
29 He X, Zeng T, Cherniakov M. Signal detectability in SS-BSAR with GNSS non-cooperative transmitter. IEE Proc Radar Sonar Navig, 2005, 152: 124–132
30 Liu F, Antoniou M, Zeng Z, et al. Point spread function analysis for BSAR with GNSS transmitters and long dwell times: theory and experimental confirmation. IEEE Geosci Remote Sens Lett, 2013, 10: 781–785
31 Cherniakov M, Zeng T, Plakidis E. Analysis of space-surface interferometric bistatic radar. In: Proceedings of IEEE International Conference on Geoscience and Remote Sensing Symposium (IGARSS), Toulouse, 2003. 778–780
32 Antoniou M, Liu F, Zeng Z. Coherent change detection using GNSS-based passive SAR: first experimental results. In: Proceedings of IET International Conference on Radar Systems, Glasgow, 2012. 1–5
33 Saini R, Zuo R, Cherniakov M. Problem of signal synchronisation in space-surface bistatic synthetic aperture radar based on global navigation satellite emissions—experimental results. IET Radar Sonar Navig, 2010, 4: 110–125
34 Tsui J. Fundamentals of Global Positioning System Receivers: A Software Approach. John Wiley & Sons, 2005
35 Dow J M, Neilan R E, Rizos C. The international GNSS service in a changing landscape of global navigation satellite systems. J Geodesy, 2009, 83: 191–198
36 Soumekh M. Synthetic Aperture Radar Signal Processing. New York: Wiley-Interscience, 1999
37 Liu F, Liu H, Hu C. Modified range migration algorithm in SS-BSAR. In: Proceedings of IET International Radar Conference, Guilin, 2009. 1–4
38 Antoniou M, Cherniakov M, Hu C. Space-surface bistatic SAR image formation algorithms. IEEE Trans Geosci Remote Sens, 2009, 47: 1827–1843
39 Zeng Z, Antoniou M, Zhang Q. Multi-perspective GNSS-based passive BSAR: Preliminary experimental results. In: Proceedings of International Radar Symposium (IRS), Dresden, 2013. 467–472
40 Huang L, Qiu X, Hu D, et al. Focusing of medium-earth-orbit SAR with advanced nonlinear chirp scaling algorithm. IEEE Trans Geosci Remote Sens, 2011, 49: 500–508
41 Preiss M, Gray D A, Stacy N J S. Detecting scene changes using synthetic aperture radar interferometry. IEEE Trans Geosci Remote Sens, 2006, 44: 2041–2054
42 Scheuchl B, Ullmann T, Koudogbo F. Change detection using high resolution Terrasar-X data—preliminary results. In: Proceedings of ISPRS Hannover Workshop, Hannover, 2009. 1–4
43 Rignot E J, van Zyl J J. Change detection techniques for ERS-1 SAR data. IEEE Trans Geosci Remote Sens, 1993, 31: 896–906
44 Zhang Q, Antoniou M, Chang W, et al. Spatial decorrelation in GNSS-based SAR coherent change detection. IEEE Trans Geosci Remote Sens, 2015, 53: 219–228
45 Zeng T, Ao D, Hu C, et al. Multi-angle BiSAR images enhancement and scatting characteristics analysis. In: Proceedings of International Conference on Radar, Lille, 2014. 1–5
46 Bradaric I, Capraro G T, Weiner D D, et al. Multistatic radar systems signal processing. In: Proceedings of IEEE Conference on Radar, Verona, 2006. 106–113